2024 European Control Conference (ECC)
June 25-28, 2024. Stockholm, Sweden

Fault detection in gauge-sensorized strain wave gears

Julian Kißkalt[1], Andreas Michalka[1], Christoph Strohmeyer[2], Maik Horn[2], Knut Graichen[1]

***Abstract*— Strain wave gears (SWG) are employed in most robot joints, and hence monitoring their condition gets more important in robotic applications. The condition of SWGs can, e.g., be observed by sensor signals of strain gauges that are mounted on the flex spline, the deformable part of the gear, for torque prediction purposes. In this paper, the feasibility of utilizing these sensor signals for fault detection in SWGs is shown and meaningful features tailored to a specific sensor setup are proposed. As a first important step towards fault detection in a real world application, synthetically generated sensor signals are considered that are derived from a simulation chain allowing the injection of different faults. In total, five distinct and practically relevant faults are considered and different algorithms are applied to classify them. In addition, robustness regarding disturbed synthetic data is investigated and the classifiers' potential for out-of-distribution prediction is evaluated.**

I. Introduction

Strain wave gears (SWG) play a key role for the motion of robot joints. Therefore, the malfunction of SWGs can lead to severe errors in robotic processes. Since SWGs are susceptible to wear and degradation [1], their condition should continuously be monitored to detect faulty and abnormal behavior in an early stage.

The setup of an SWG is illustrated in Fig. 1. The input shaft is connected to the so-called wave generator (WG) that deforms, with its elliptical shape, the elastic flex spline and pushes the flex spline teeth at the major axis of the ellipse into the teeth of the circular spline [2]. The circular spline is equipped with a few more teeth than the flex spline and therefore by the rotation of the WG, the relative angle between the flex spline and the circular spline changes accordingly. Since the relative angle between the two parts changes only slightly, high transmission ratios can be realized by SWGs [3].

To model faults, anomalies, or degradation in SWGs, different approaches can be found in the literature. E.g. in [4], the impact of degradation on the stiffness of the gear as well as its hysteresis behavior is modeled. In [5], a high-fidelity multibody model of a collaborative robot, including a detailed model of the SWGs in the joints, is presented with the aim of performing condition monitoring. Zhang et al. [6] analyze the reliability of failure, in particular of so-called strength failures that can, e.g., lead to the fracture of the flex spline, and of a so-called stiffness degradation failure that impacts the performance of the SWG.

[1] Julian Kißkalt, Andreas Michalka & Knut Graichen are with the Chair of Automatic Control, Friedrich-Alexander-Universität Erlangen-Nürnberg, Erlangen, Germany {julian.kisskalt,andreas.michalka, knut.graichen}@fau.de

[2] Christoph Strohmeyer & Maik Horn are with Schaeffler Technologies AG & Co. KG, Herzogenaurach, Germany {christoph.strohmeyer,maik.horn}@schaeffler.com

Fault detection in SWGs is covered, e.g., in [7], where faults in different SWGs located at different positions in the robot are distinguished based on acceleration sensor signals. Moreover, Kuo et al. [8] record the sound of SWGs by a microphone and use these data to classify between a faulty and a healthy state of the gear. Finally, according to [9], the electrical current of the motor driving the SWG can also be used to distinguish between healthy and faulty behavior of the gear.

To avoid an additional torque sensor in the joint of the robot, torque information can be extracted from the deformation of the flex spline by means of strain gauges [10], [11], see Fig. 1. The sensor signals of these strain gauges can be synthetically generated by means of the simulation chain introduced and validated by measurement data in [12]. The simulation chain consists of three submodels: first, a model describing the dynamic behavior of the SWG taken from [13]; second, a space truss model to compute the deformation of the flex spline; and third, a model of the strain gauge sensors mounted on it. In addition, the opportunities to inject practically relevant faults in the simulation chain is shown.

In this paper, the feasibility to leverage sensor signals of strain gauges, initially mounted on the flex spline for torque prediction, to detect faults in SWGs is presented. Furthermore, significant features for a specific sensor setup are suggested for this task. As a first important step towards real world applications, synthetically generated, but realistic measurement data showing frequently observed faults in practical experiments are used for this analysis. The data is generated with the simulation chain presented and validated in [12]. In contrast to the aforementioned literature, the simulation chain creates the opportunity to consider multiple variations of the same fault in one SWG and also to examine the behavior of different SWGs showing these faults. Moreover, the performance of different classifiers applied to the generated data is evaluated, their robustness against disturbances in this data is tested, and their ability for out-of-distribution prediction is studied.

This paper is organized as follows: Section II introduces the faults considered for the fault detection. Topics regarding the setup of the fault detection analyses, i.e. the generation of the data set and the extraction of features, are exemplified in Section III. Subsequently, the results of the fault detection are presented in Section IV. Finally, conclusions are given in Section V.

II. Simulation Chain and Considered Faults

In this work, gauge-sensorized SWGs are considered similar to the one shown in Fig. 1. To generate synthetic sensor signals of these gears, the simulation chain presented

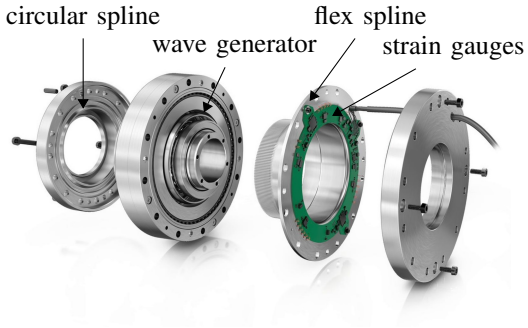

Fig. 1: Setup of the gauge-sensorized strain wave gear RT1-T from Schaeffler [14], edited.

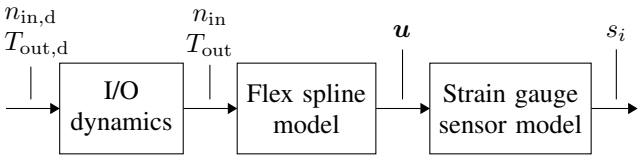

Fig. 2: Flow chart of the simulation chain.

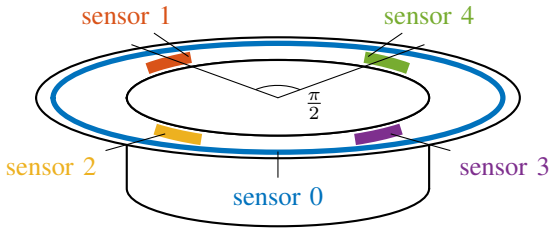

Fig. 3: Layout of sensors 0 to 4 at the back of the flex spline's collar.

TABLE I: Considered faults and manipulated model for their injection.

Fault category	Manipulated model
Reduced damping	I/O dynamics
Reduced stiffness	I/O dynamics
Eccentric WG	Flex spline
Root tooth crack	Flex spline
Tip tooth crack	Flex spline

in [12] is used, which consists of three different models, as illustrated in Fig. 2. The first part is a dynamic input/output (I/O) model of the SWG according to [13], with an imposed operating point specified by the desired rotation speed $n_{\mathrm{in,d}}$ and the desired load torque $T_{\mathrm{out,d}}$ at the input and output side of the gear, respectively, see Fig. 2. From the dynamic I/O model, the acting rotational speed n_{in} and the acting output torque T_{out} are extracted and used to derive the loads in the flex spline model. The flex spline is represented by a space truss and computes the displacement vector $\boldsymbol{u}$ containing the displacements of every discrete node in every spatial direction. Thereafter, the displacement vector $\boldsymbol{u}$ is used in the strain gauge sensor model to compute the signals s_i of strain gauge sensors of the given specific layout shown in Fig. 3. All sensor signals $s_i, i \in \{0, 1, \ldots, 4\}$ are normalized voltages of unit $\mathrm{mV/V}$ and represent the output of the whole simulation chain.

The simulation chain is validated by measurements in [12]. In this work, five different fault categories are considered, see Table I. The following lines compactly exemplify the dynamic I/O model and the flex spline model to illustrate the injection of the single faults.

A. *Faults in the dynamic I/O model*

The dynamic I/O model of the SWG introduced in [13] can be described by differential equations of the form

$$\ddot{\boldsymbol{\varphi}} = \boldsymbol{f}(\boldsymbol{\varphi}, \dot{\boldsymbol{\varphi}}, n_{\mathrm{in,d}}, T_{\mathrm{out,d}}), \qquad \boldsymbol{\varphi} = \begin{bmatrix} \varphi_{\mathrm{in}} \\ \varphi_{\mathrm{out}} \end{bmatrix}, \tag{1}$$

with φ_{in} and φ_{out} being the angular position of the gear's input and output shaft, respectively. The dynamic model (1) considers the stiffness of the whole gear by linear and cubic stiffness effects with respect to $\Delta\varphi_k$ leading to the stiffness torque [13]

$$T_{\mathrm{stiff}} = k_1 \Delta\varphi_k + k_2 \left(\Delta\varphi_k\right)^3, \tag{2}$$

with the linear and cubic stiffness coefficients k_1, k_2, and the nonlinear twist

$$\Delta\varphi_{\mathrm{k}} = \tan\alpha_{\mathrm{in}} \left(\varphi_{\mathrm{in}} - \varphi_{\mathrm{out}}\right) + \frac{\varphi_{\mathrm{out}}}{\tan\alpha_{\mathrm{tooth}}} + \varphi_{\mathrm{err}}, \tag{3}$$

with the kinematic error profile φ_{err} and

$$\alpha_{\mathrm{in}} = \arctan\left(\frac{1}{(N+1)\tan\alpha_{\mathrm{tooth}}}\right), \tag{4}$$

with the gear-tooth angle α_{tooth} and the catalog gear ratio N.

Friction effects in the dynamic model (1) include constant as well as linear and cubic friction forms. Moreover, friction caused by resonance vibration and Coulomb friction are modeled, which leads in total to the friction torque [13]

$$T_{\mathrm{fric}} = b_0 + b_1\dot{\varphi}_{\mathrm{b}} + b_2\dot{\varphi}_{\mathrm{b}}^3 + b_3 \sin(\varphi_{\mathrm{out}} + \theta_{\mathrm{b}}) + \mu F_{\mathrm{n}}, \tag{5}$$

with the damping coefficients b_1, b_2, b_3, the phase shift θ_{b}, the Coulomb friction coefficient μ, the gear-tooth normal force F_{n}, and

$$\dot{\varphi}_{\mathrm{b}} = -\frac{\dot{\varphi}_{\mathrm{out}}}{\sin\alpha_{\mathrm{tooth}}}. \tag{6}$$

The faults that are subsequently injected into the dynamic I/O model are derived from physical effects that are seen in real world experiments. One aspect that can be observed is the increase of the efficiency η in the first hundred hours of the operating time. A comparable behavior is mentioned in the literature, e.g., in [6]. The reason for the increase of efficiency in real world applications is assumed to be run-in effects in the first hundred hours of operating time that correspond to degradation processes. In addition, this can lead to some backlash in the gear.

The efficiency can be computed by $\eta = {}^{P_{\mathrm{out}}}/_{P_{\mathrm{in}}}$, with P_{in} and P_{out} being the mechanical power at the input and output of the SWG, respectively. In this work, the mean value of η

TABLE II: Temporal evolution of the efficiency η in experiments and its reproduction by the simulation chain with the nominal damping coefficient b_1^{nom} in $\mathrm{Nms/rad}$.

	Experiments		Simulations	
	0 h	250 h	$b_1 = b_1^{\mathrm{nom}}$	$b_1 = \frac{1}{3} b_1^{\mathrm{nom}}$
η [%]	56.51	66.76	65.81	73.43

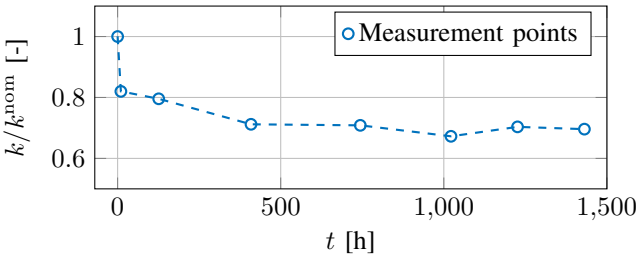

Fig. 4: Temporal evolution of measured SWG stiffness k normalized with the nominal stiffness k^{nom} in $\mathrm{Nm/rad}$ measured in the beginning of the experiment.

in a certain time interval is determined for a specific input rotation speed $\dot{\varphi}_{\mathrm{in}}$ and load torque T_{out}. Table II lists the efficiency η for a gear in its initial state and after 250 h of operating time. The comparison of these two values shows that the efficiency η has increased by approx. 10 % in the first 250 h of the operating time. This behavior is also observed for measurement data of other SWGs of the same type.

The simulation chain exhibits a similar behavior if the linear damping parameter b_1 in (5) is decreased, which is also exemplified in Table II. In particular, decreasing the damping parameter b_1 by $1/3$ results in an increase of the efficiency η by approx. 7 %.

Another observation that can be made is the decrease of the stiffness of the SWG over time. This is also confirmed by [6]. As an example, the temporal evolution of the measured stiffness of a SWG is shown in Fig. 4, where the stiffness drops by approx. 20 % in the first 10 h. Afterwards, the stiffness stays roughly constant. The reason for this behavior is again assumed to be run-in effects. The simulation chain is also able to exhibit a decrease of the SWG stiffness. This is done, e.g., by reducing the linear stiffness coefficient k_1 in (2) of the dynamic I/O model of the SWG.

The decrease of the damping and of the stiffness are each considered as one fault class, see Table I.

B. Faults in the flex spline model

The flex spline in [12] is modeled as space truss. The geometry of the flex spline is discretized by a multitude of nodes that are connected with elastic bars of stiffness k_{bar}, see Fig. 5. The space truss model has to satisfy certain boundary conditions that can be derived from the design of the gear. The first one is the fixation of the flex spline to the housing of the gear, which imposes a zero displacement of the nodes located on the edge of the collar, see Fig. 5. Furthermore, the flex spline's sleeve is deformed due to the elliptical shape of the WG. This leads to the predefined displacement $\boldsymbol{u}_{i,\mathrm{elliptical}}$ of the inside nodes of the sleeve being in contact with the wave generator. Finally, the tooth meshing forces $\boldsymbol{F}_{\mathrm{tooth},i}$ act on the nodes at the outside of the sleeve where the flex spline teeth are located.

As listed in Table I, the fault categories eccentric WG, root tooth crack, and tip tooth crack are considered. The relevance of the last two faults is also pointed out in [15]. The injection of these three faults in the simulation chain is exemplified in [12] and is subsequently summarized briefly. The eccentric WG fault is realized by adding some eccentric displacement $\boldsymbol{u}_{\mathrm{ecc}} = \left[r, \theta, 0\right]^{\mathsf{T}}$ in cylindrical coordinates with radius r and angle θ to the displacement $\boldsymbol{u}_{i,\mathrm{ellipitcal}}$, as shown in Fig. 5. To obtain a root tooth crack, the stiffness k_{bar} between neighboring nodes in circumferential direction is reduced drastically to $\tilde{k}_{\mathrm{bar}}$. Finally, a tip tooth crack is modeled by a strongly reduced tooth force $\tilde{\boldsymbol{F}}_{\mathrm{tooth},i}$ acting only at a specific node i.

C. Simulation of faults

In summary, Fig. 6 illustrates sensor signals $\tilde{s}_i$ of all five aforementioned fault classes and additionally the sensor signals s_i of a healthy gear. Decreasing the linear damping coefficient b_1 in (5) has hardly any impact on the sensor signals s_i as shown in Fig. 6a. If the linear stiffness coefficient k_1 is decreased in (2), only the sensor signal s_0 changes very slightly, as can be seen in Fig. 6b. An eccentric wave generator mainly leads to the offset of some sensor signals, e.g., sensor signals s_1 and s_3 in Fig. 6c, and additionally, to the change of their sinusoidal shape. The root tooth crack in Fig. 6d shows changing amplitudes in all sensor signals s_i. Finally, slight deviations of sensor signals s_1 and s_3 are visible between time 0.015 s and 0.02 s in case of the tip tooth crack, as can be seen in Fig. 6e.

In advance, several variants of each fault are considered and the sensor signals $\tilde{s}_i$ are compared. From this comparison it is concluded that most sensor signals $\tilde{s}_i$ shown in Fig. 6 are characteristic for each fault category. Furthermore, it is visible that the presented faults lead to different shapes of the sensor signals $\tilde{s}_i$ in Fig. 6. Hence, these sensor signals are used for fault detection purposes in the following.

III. Setup of the Fault Detection Analysis

Having introduced the simulation chain and the considered faults, the specifications of the fault detection analysis are introduced in this section. These are the selection of meaningful features, the generation of data sets for fault detection tasks, and the classifiers themselves.

A. Feature selection

The selection of features plays a key role in the context of fault detection. Usually, features cannot be directly extracted from raw measurement signals. As illustrated, e.g., in [8], [16], a lot of effort is put into the preprocessing and afterwards into the choice of features. Choosing statistical measures as features is popular for fault detection purposes in SWGs [8], [16]. Hence, the mean m_{s_i} and variance σ_{s_i} of the sensor signals s_i are considered in the following. The behavior of SWGs can vary strongly for different operating points. Hence, all features, e.g. mean and variance, are

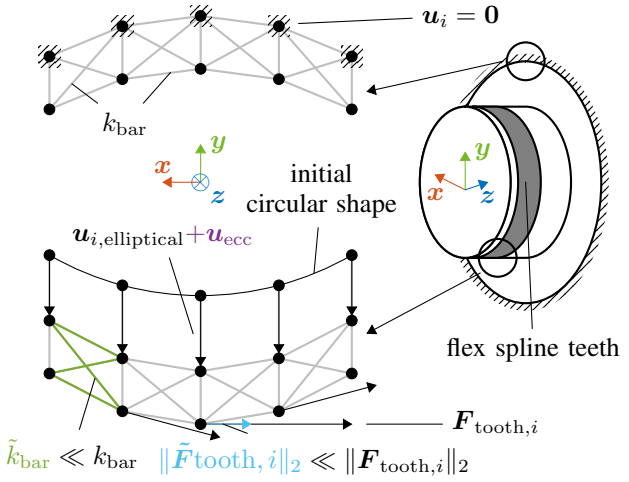

Fig. 5: Boundary conditions due to the elliptical shape of the wave generator, due to the fixation to the housing of the gear, and due to the tooth contact.

normalized for each operating point by the value of the healthy gear, e.g.,

$$m_{s_i}^{\mathrm{rel}} = \frac{m_{\bar{s}_i}}{m_{s_i}} \,. \tag{7}$$

Furthermore, due to the periodic shape of the sensor signals shown in Fig. 6, reasonable features can be the discrete Fourier transform (DFT) $\mathrm{DFT}\,(\bar{s}_i)$, see e.g. [17], of the zero-mean sensor signals $\bar{s}_i = s_i - m_{s_i}$. Exemplarily, the DFT of the zero-mean sensor signals $\bar{s}_0$ and $\bar{s}_1$ is shown in Fig. 7 with the normalization of the frequency f by the input rotation speed n_{in}. On the one hand, deviations of the DFT of sensor signal $\bar{s}_0$ in Fig. 7a are only visible for the reduced stiffness fault and the root tooth crack fault. On the other hand, only the DFT of sensor signal $\bar{s}_1$ of the eccentric WG fault differs significantly from the DFT of the healthy gear, as can be seen in Fig. 7b.

However, the DFT of the difference of certain sensor signals is a more significant feature. Due to the symmetric layout of the strain gauge sensors shown in Fig. 3 and the symmetry of the elliptical wave generator, sensor signals s_1 and s_3 as well as s_2 and s_4, respectively, have to be similar for healthy SWGs. Therefore, their differences

$$\Delta s_{1,3} = s_1 - s_3 \,, \qquad \Delta s_{2,4} = s_2 - s_4 \tag{8}$$

can contain valuable information regarding faults in SWGs, as illustrated in Fig. 7c and 7d. For the DFT of both $\Delta\bar{s}_{1,3}$ and $\Delta\bar{s}_{2,4}$, the eccentric WG fault, the root tooth crack fault, and the tip tooth crack fault can be clearly distinguished from each other as well as from the remaining curves. However, the remaining curves, corresponding to the healthy gear, the reduced damping and the reduced stiffness fault, look similar. To distinguish between these fault classes, additional features, e.g. related to the efficiency, are necessary.

The efficiency of SWGs also changes with varying operating points. Hence, the normalized quantity η^{rel} according to (7) is considered. A good distinction between slight changes in η^{rel} can be achieved by considering the expression

$$\eta_2^{\mathrm{rel}} = \sqrt[4]{|1 - \eta^{\mathrm{rel}}|} \,. \tag{9}$$

TABLE III: Considered feature selections.

Selection	Statistics	Frequency spectrum	Efficiency
1	$m_{s_i}^{\mathrm{rel}}$, $\sigma_{s_i}^{\mathrm{rel}}$	-	η^{rel}
2	$m_{s_i}^{\mathrm{rel}}$, $\sigma_{s_i}^{\mathrm{rel}}$	$\mathrm{DFT}^{\mathrm{rel}}\,(\bar{s}_i)$	η^{rel}
3	-	$\mathrm{DFT}^{\mathrm{rel}}\,(\Delta\bar{s}_{1,3})$, $\mathrm{DFT}^{\mathrm{rel}}\,(\Delta\bar{s}_{2,4})$	η_2^{rel}

The different feature selections considered in this work are listed in Table III. The DFT features are normalized component-wise similar to (7) resulting in $\mathrm{DFT}^{\mathrm{rel}}\,(\bullet)$. Selection 1 considers only statistical measures and the relative efficiency η^{rel}. Selection 2 additionally takes the DFT of all sensor signals into account to study their benefit as features. Finally, Selection 3 consists of the DFT of the difference of redundant sensor signals $\mathrm{DFT}\,(\Delta\bar{s}_{1,3})$ and $\mathrm{DFT}\,(\Delta\bar{s}_{2,4})$ as well as the special efficiency expression η_2^{rel}, since this selection shows good classification results in simulation studies done in advance.

B. Data set

The data of three different SWG models is considered in this study. For this reason, the dynamic I/O model is, at first, parameterized with the parameters proposed in [13] and thereafter the healthy linear damping parameter b_1 and the healthy linear stiffness parameter k_1 are varied for each gear according to Table IV. The strain gauge sensor model of each SWG model is additionally fitted to measurement data of three distinct Schaeffler RT1-T gears, see Fig. 1, according to [12]. SWG models 1, 2, and 3, therefore, differ in several properties from each other.

Next, the fault classes presented in Section II are considered including an additional healthy class, which leads to in total six classes. Sixty different variants of the fault are considered in each fault class. This is done for each of the SWG models 1, 2, and 3. The variants of the fault classes are listed in Table V. Sixty different variants of the damping parameter $\tilde{b}_1$ and the stiffness parameter $\tilde{k}_1$ are considered in the reduced damping and reduced stiffness class, respectively. Furthermore, sixty data points for the eccentric WG, the root tooth crack, and the tip tooth crack class are generated by applying each fault with three different degrees of severity, and additionally, at twenty different, equally distributed positions in circumferential direction, see Table V. In case of the healthy class, sixty times the same SWG model is considered to balance the number of data points in this class compared to the other ones.

Finally, the data is generated for six operating points by considering every combination of the desired input rotation speeds $n_{\mathrm{in,d}} \in \{2000, 4000\}$ rpm and the desired load torques $T_{\mathrm{out,d}} \in \{7, 39, 70\}$ Nm. Therefore, a number of overall 2160 data points are considered for each of the three SWG models, leading to 6480 data points in total.

A disturbed data set, similar to the aforementioned one, is also generated since slight irregularities can be seen in

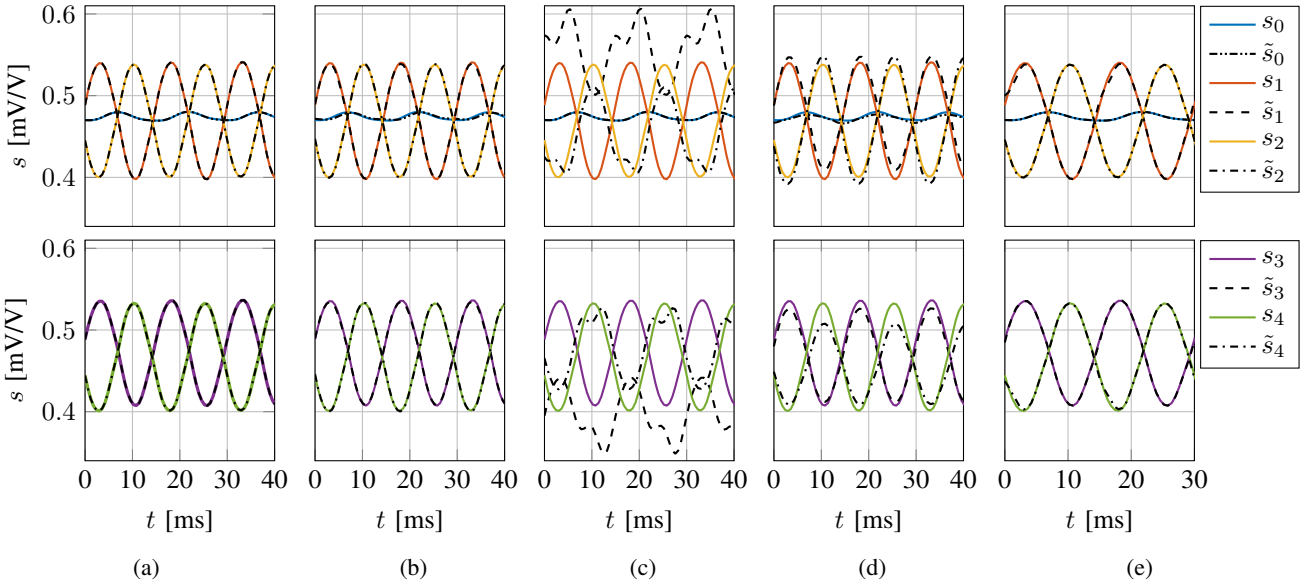

Fig. 6: Healthy and faulty sensor signals s_i and $\tilde{s}_i$, respectively, for the faults: (a) reduced damping, (b) reduced stiffness, (c) eccentric WG, (d) root tooth crack, and (e) tip tooth crack.

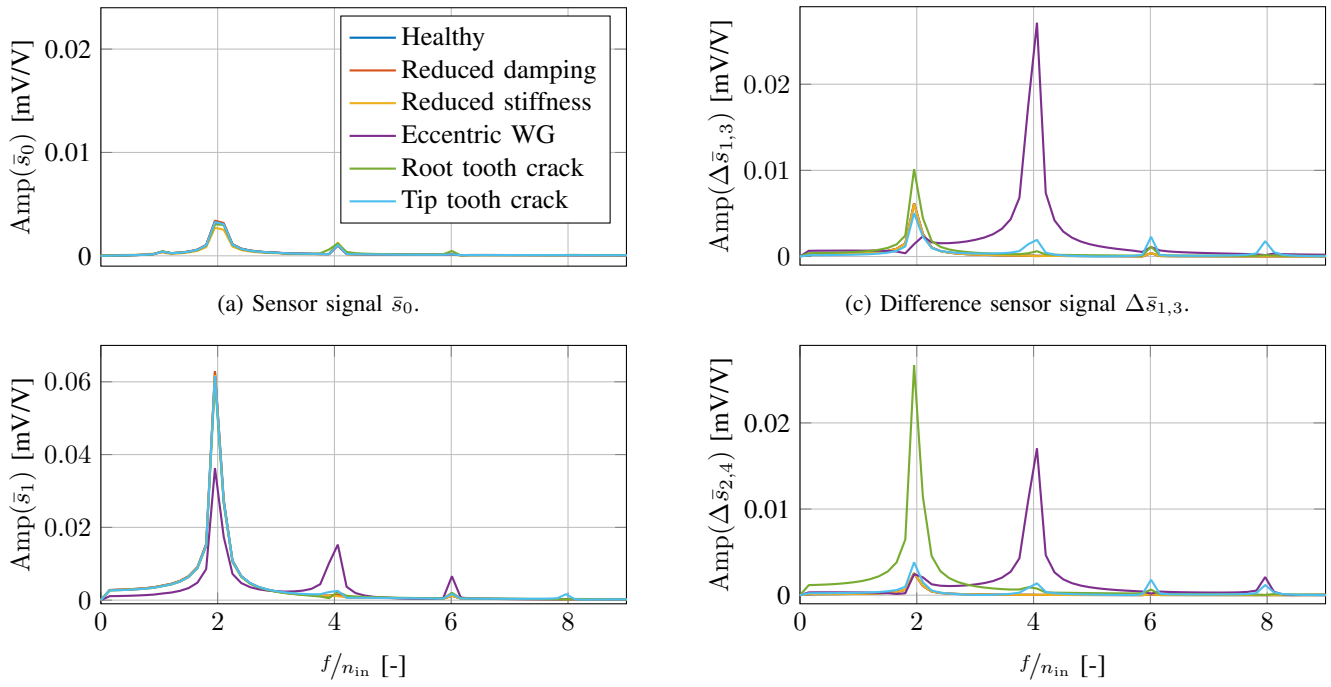

Fig. 7: DFT of different sensor signals.

measurement data. It can be observed that these irregularities have the shape of lower order harmonics of the input rotation speed and that slight constant offsets occur. Therefore, for each sensor signal s_i, randomly chosen amplitudes a_j and phases α_j are generated and a harmonic disturbance is added to the sensor signals according to

$$s_i^{\mathrm{d}} = s_i + a_0 + \sum_{j=1}^{4} a_j \sin\left(\frac{2\pi}{j} n_{\mathrm{in}} t + \alpha_j\right) . \tag{10}$$

An example of disturbed sensor signals s_i^{d} can be seen in Fig. 8. The disturbed data set consists as well of 6480 data points.

C. Applied classification algorithms

The implementations of Python's Scikit-learn package [18] are used for the following classification tasks. The considered classifiers are chosen to be a multi-layer perceptron (MLP), a support vector machine (SVM), a random forest classifier (RF), a k-nearest neighbor classifier (KNN), and a naive

TABLE IV: Parameters of considered SWG models.

SWG model	b_1	k_1
1	b_1^{nom}	k_1^{nom}
2	$b_1^{\mathrm{nom}} \cdot 1.2$	$k_1^{\mathrm{nom}} \cdot 1.2$
3	$b_1^{\mathrm{nom}} \cdot 0.8$	$k_1^{\mathrm{nom}} \cdot 0.8$

TABLE V: Specification of sixty variants in each class.

Class	Properties
Healthy	SWG model not varied
Reduced damping	$\tilde{b}_1 = \lambda_j \cdot b_1$, with 60 evenly spaced λ_j between 0.4 and 0.8
Reduced stiffness	$\tilde{k}_1 = \lambda_j \cdot k_1$, with 60 evenly spaced λ_j between 0.4 and 0.8
Eccentric WG	$\boldsymbol{u}_{\mathrm{ecc}} = \left[r_j, \theta, 0\right]^{\mathsf{T}}$, $j = 1, ..., 3$, $\theta = 0, \pi/10, ..., 19\pi/10$
Root tooth crack	$\tilde{k}_{\mathrm{bar}} = \lambda_j \cdot k_{\mathrm{bar}}$, $\lambda_j \ll 1$, $j = 1, ..., 3$, at $\theta = 0, \pi/10, ..., 19\pi/10$
Tip tooth crack	$\|\tilde{\boldsymbol{F}}_{\mathrm{tooth},i+j}\|_2 = \lambda_k \cdot \|\boldsymbol{F}_{\mathrm{tooth},i+j}\|_2$, $\lambda_k \ll 1$, $k = 1, ..., 3$, $j = 1, ..., 20$

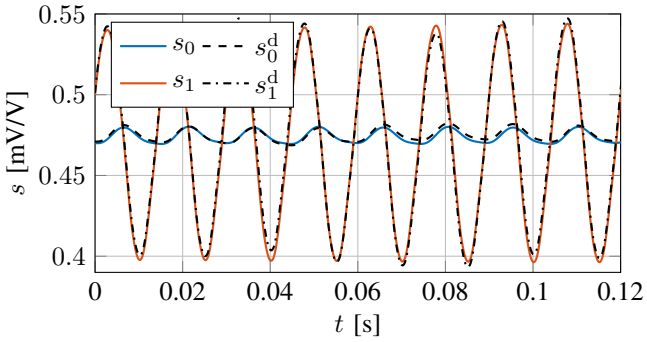

Fig. 8: Comparison of non-disturbed and disturbed data.

TABLE VI: Properties and architecture of chosen classifiers.

Classifier	Properties
MLP: Multi-layer perceptron	3 hidden layers, 10 neurons each, ReLU activation functions
SVM: Support vector machine	Radial basis function kernel
RF: Random forest	100 trees of depth 7
KNN: k-nearest neighbors	3 considered neighbors
NB: Naive bayes	Gaussian distribution assumed

bayes classifier (NB), see e.g. [17], [19]. Their properties are listed in Table VI and relate mainly to the standard settings of the implementations of Python's Scikit-learn package, however some adaptions are made and are reasoned in the following.

An analysis is made for MLP in advance to investigate the influence of the number of neurons per hidden layers and the number of hidden layers themselves. For this reason, $\{2, 3, 4\}$ hidden layers are considered with $\{10, 30, 50\}$ neurons per layer and the architecture showing the best results for Selection 3 on disturbed data is chosen. Multiple kernels have been tested for SVM, but, the most promising polynomial kernels have been rejected due to unreasonably long training times with only slightly improved results at the same time. The performance of RF converges for an increasing number of trees and an increasing depth of each tree. The size of RF was in advance slowly raised and chosen in such a way that a further increase does not lead to significantly improved classification results anymore. The number of considered neighbors for KNN is varied and the one with the best results for Selection 3 on disturbed data is chosen. Finally, a Gaussian distribution is taken for NB since it is assumed that it suits best to the distribution of the data points.

IV. Fault Detection Analyses

In this section, the fault detection on the data set presented in the previous section is carried out. Furthermore, the robustness of the classification is evaluated by considering disturbed data and performing out-of-distribution classification. To reduce the impact of unfortunate choices of training and test sets, a k-fold cross validation [20] with four splits is applied and the average score over all splits is compared in the following.

A. Varying feature selection

First of all, the influence of the feature selections listed in Table III on the classification score is evaluated in Table VII. There, the RF and the KNN classifiers show similar scores on Selection 1 and 2 with a test score of almost $100\,\%$ and approx. $97\,\%$, respectively. However, on Selection 3, they show their lowest test scores of about $97\,\%$ and $94\,\%$, respectively. On the other hand, MLP shows its highest test score of approx. $98\,\%$ on Selection 3 in contrast to less than $84\,\%$ on the other selections. Reasonable test scores of about $93\,\%$ on Selection 1 are achieved by NB. Yet, on the other selections, the test score is below $80\,\%$. The last place is taken by SVM exhibiting a test score of about $66\,\%$ on Selection 3.

Based on the presented results, RF seems to be the most promising classifier regarding its prediction score and its abilities to predict reliably with different selections. For KNN, similar findings hold, however, with a smaller classification score. MLP also seems to be promising, but only if the features of Selection 3 are chosen. The highest scores are achieved using Selection 1 or 3 for all classifiers. Hence, it can be concluded that the DFT of single sensor signals does not improve the classification results in these cases.

B. Disturbed data

The performance of the classifiers is now evaluated on the disturbed data set. For this reason the classifiers are trained and tested on the disturbed data, similar to the aforementioned analysis. The corresponding prediction results are listed in Table VIII. In general, the prediction scores are not

TABLE VII: Score on training and test set for different selections.

	MLP	SVM	RF	KNN	NB
Selection 1					
Avg. training score [%]	84.17	49.77	99.92	98.91	92.64
Avg. test score [%]	83.33	49.60	**99.81**	**97.95**	**92.59**
Selection 2					
Avg. training score [%]	82.47	35.60	99.56	98.62	79.96
Avg. test score [%]	81.10	35.49	**99.24**	**97.21**	79.89
Selection 3					
Avg. training score [%]	99.09	83.51	98.21	97.92	79.49
Avg. test score [%]	**98.30**	66.10	**96.96**	**94.48**	79.43

TABLE VIII: Score on training and test set for disturbed data.

	MLP	SVM	RF	KNN	NB
Selection 1					
Avg. training score [%]	67.14	47.29	91.63	89.20	74.17
Avg. test score [%]	66.02	47.15	**90.35**	79.69	73.72
Selection 2					
Avg. training score [%]	71.34	27.02	92.80	87.56	67.57
Avg. test score [%]	69.43	27.16	**91.88**	78.60	66.81
Selection 3					
Avg. training score [%]	99.23	86.56	98.35	81.34	70.61
Avg. test score [%]	**98.24**	46.20	**96.88**	63.38	69.72

as high as they are in the undisturbed case. For MLP and RF, the test score on Selection 3 decreases only slightly. However, the score of RF drops by approx. $7\,\%$ and $9\,\%$ for the other selections. The test score of KNN and NB decline in all cases more strongly than the score of RF. The best test score that can be achieved by KNN is about $80\,\%$ on Selection 1. In case of NB, the highest test score is about $73.72\,\%$ on the same selection. Again, the lowest test scores are achieved by SVM with a maximum test score of approx. $47\,\%$.

Therefore, it is summarized, that the MLP and RF classifiers show the best robustness against disturbances. The feature selection that contributes the most to this result is Selection 3, which takes the redundancy of the sensor signals into account.

C. Out-of-distribution classification

In real world applications, the classifiers cannot be trained on every gear to which they will be applied to in future. Thus, the classification on data of simulation chains that have not been used for the training of the classifier is considered. The classifiers are subsequently trained for this reason on two of the simulation chains mentioned in Table IV, e.g., SWG models 1 and 2, afterwards, the prediction is done on data of the remaining simulation chain, in this example the data of SWG model 3. This case is named $1, 2 \rightarrow 3$ in Table IX,

TABLE IX: Avg. score in per cent on out-of-distribution classification.

	MLP	SVM	RF	KNN	NB
Selection 1					
$1, 2 \rightarrow 3$	70.74	44.44	**92.50**	90.14	**91.99**
$2, 3 \rightarrow 1$	75.83	48.15	**99.91**	87.82	**92.69**
$1, 3 \rightarrow 2$	75.37	43.84	**93.56**	86.30	**86.16**
Selection 2					
$1, 2 \rightarrow 3$	61.16	31.99	59.54	87.36	76.30
$2, 3 \rightarrow 1$	59.54	30.32	90.93	80.88	79.91
$1, 3 \rightarrow 2$	58.98	30.65	61.76	83.33	67.92
Selection 3					
$1, 2 \rightarrow 3$	79.81	40.93	82.82	77.08	77.73
$2, 3 \rightarrow 1$	81.62	48.75	77.82	65.97	60.28
$1, 3 \rightarrow 2$	74.21	47.92	85.79	83.15	67.55

which lists the score of this classification task for all possible variants.

In this setting, the best results are achieved by RF with a score above $92\,\%$ on Selection 1 in all cases. NB achieves also reasonable results on the same selection with a score between $86\,\%$ and $93\,\%$ followed by KNN with a score between $86\,\%$ and approx. $90\,\%$. The highest score of MLP is approx. $82\,\%$ on Selection 3. SVM performance is the weakest with the best score of approx. $48\,\%$ on Selection 1 and approx. $49\,\%$ on Selection 3.

Hence, regarding the out-of-distribution classification, RF and NB are the best performing algorithms when considering Selection 1. Although, MLP looked promising on the classification of disturbed data, the quality of this classifier is not as high when doing out-of-distribution classification.

D. Out-of-distribution classification on disturbed data

The out-of-distribution classification is done on the disturbed data in this section to study the worst case quality of the fault classification that is assumed to be expected on real world measurement data. Both training and testing are executed as described in the previous paragraphs.

The classification scores of the four most promising classifiers, MLP RF, KNN, and NB on the most promising selections, Selection 1 and 3, are listed in Table X. RF achieves the best classification scores on Selection 3, which vary between approx. $86\,\%$ and $93\,\%$. RF still achieves scores between approx. $79\,\%$ and $88\,\%$ on Selection 1. Moreover, the classification score of MLP varies in the best case between approx. $72\,\%$ and $83\,\%$. The other classifiers achieve classification scores smaller than $75\,\%$.

This analysis shows that RF achieves the best results for the out-of-distribution classification on disturbed data. The classification score is above $86\,\%$ in all considered cases. However, the results have to be rated in context of a specific application task. It is assumed that usually the achieved score is not sufficient. Therefore, the potential of retraining the classifiers has to be evaluated, e.g., by applying transfer learning concepts.

TABLE X: Avg. score in per cent on out-of-distribution classification on disturbed data for four selected classifiers.

	MLP	RF	KNN	NB
Selection 1				
$1, 2 \rightarrow 3$	51.25	87.59	70.93	66.85
$2, 3 \rightarrow 1$	53.70	85.69	71.67	65.00
$1, 3 \rightarrow 2$	61.30	79.03	65.65	73.84
Selection 3				
$1, 2 \rightarrow 3$	72.08	**90.09**	56.99	53.94
$2, 3 \rightarrow 1$	82.92	**86.20**	47.31	56.39
$1, 3 \rightarrow 2$	82.87	**92.31**	50.32	74.26

V. Conclusions

Fault detection in gauge-sensorized strain wave gears (SWG) using synthetically generated strain gauge sensor signals is presented in this paper. Five fault classes and a healthy class are distinguished and the performance as well as the robustness of different classifiers is compared.

This paper points out the practicality of fault detection in SWGs based on strain gauge sensors of a specific layout. Furthermore, simple but meaningful features are proposed for this task. The fault detection analysis shows that regardless of the feature selection, the random forest classifier (RF) is the most promising classifier with test scores up to $99.81\,\%$. In addition, the multi-layer perceptron (MLP) shows a high test score of $98.30\,\%$ as well, but only using the features of Selection 3. The consideration of disturbed sensor signals leads to the conclusion that a reasonable classification score above $96\,\%$ on the test set is only achieved by MLP and RF using the features of Selection 3. For the out-of-distribution classification, scores above $92\,\%$ in all considered cases can only be achieved by RF. Finally, analyzing the classification quality on disturbed out-of-distribution data leads to the conclusion that among the considered classifiers, RF is the most robust one achieving a classification score of at least $86.20\,\%$.

In future work, more data sets of different gears are to be considered and analyzed regarding the robustness of the classifiers. In addition, the impact of the architecture and size of MLP and RF on their robustness properties is to be evaluated. Furthermore, methods for relearning, e.g., considering transfer learning algorithms, are to be developed to tackle the problem of out-of-distribution classification. Finally, regarding real world applications, the analyses are to be done with measurement data and the online applicability of the presented classifiers on microcontrollers is to be studied. A test bench is currently under construction for this reason.

VI. Acknowledgements

This work has been supported by the Schaeffler Hub for Advanced Research at Friedrich-Alexander-Universität Erlangen-Nürnberg (SHARE at FAU).

References

[1] I. Schafer, P. Bourlier, F. Hantschack, E. Roberts, S. Lewis, D. Forster, and C. John, "Space lubrication and performance of harmonic drive gears," in *Proc. of 11th European Space Mechanisms and Tribology Symposium*, vol. 591, 2005, pp. 65–72.

[2] F. H. Ghorbel, P. S. Gandhi, and F. Alpeter, "On the kinematic error in harmonic drive gears," *Journal of Mechanical Design*, vol. 123, no. 1, pp. 90–97, 2001.

[3] C. Zou, T. Tao, G. Jiang, X. Mei, and J. Wu, "A harmonic drive model considering geometry and internal interaction," *Proc. of the Institution of Mechanical Engineers, Part C: Journal of Mechanical Engineering Science*, vol. 231, no. 4, pp. 728–743, 2017.

[4] T. Tang, H. Jia, J. Li, J. Wang, and X. Zeng, "Modeling of transmission compliance and hysteresis considering degradation in a harmonic drive," *Applied Sciences*, vol. 11, no. 2, p. 665, 2021.

[5] A. Raviola, R. Guida, A. C. Bertolino, A. De Martin, S. Mauro, and M. Sorli, "A comprehensive multibody model of a collaborative robot to support model-based health management," *Robotics*, vol. 12, no. 3, p. 71, 2023.

[6] X. Zhang, G. Jiang, H. Zhang, X. Yun, and X. Mei, "Reliability analysis for dependent competing failure of harmonic drive with strength failure and stiffness degradation failure," *Engineering Computations*, vol. 38, no. 10, pp. 3645–3672, 2021.

[7] G. Yang, H. Tao, R. Du, and Y. Zhong, "Compound fault diagnosis of harmonic drives using deep capsule graph convolutional network," *IEEE Transactions on Industrial Electronics*, vol. 70, no. 4, pp. 4186–4195, 2022.

[8] J.-Y. Kuo, C.-Y. Hsu, P.-F. Wang, H.-C. Lin, and Z.-G. Nie, "Constructing condition monitoring model of harmonic drive," *Applied Sciences*, vol. 12, no. 19, p. 9415, 2022.

[9] I. Raouf, H. Lee, Y. R. Noh, B. D. Youn, and H. S. Kim, "Prognostic health management of the robotic strain wave gear reducer based on variable speed of operation: A data-driven via deep learning approach," *Journal of Computational Design and Engineering*, vol. 9, no. 5, pp. 1775–1788, 2022.

[10] M. Hashimoto and Y. Kiyosawa, "Experimental study on torque control using harmonic drive built-in torque sensors," *Journal of Robotic Systems*, vol. 15, no. 8, pp. 435–445, 1998.

[11] B. Jung, B. Kim, J. C. Koo, H. R. Choi, and H. Moon, "Joint torque sensor embedded in harmonic drive using order tracking method for robotic application," in *IEEE/ASME Transactions on Mechatronics*, vol. 22, no. 4, 2017, pp. 1594–1599.

[12] J. Kißkalt, A. Michalka, C. Strohmeyer, M. Horn, and K. Graichen, "Simulation chain for sensorized strain wave gears," in *Proc. of 27th International Conference on System Theory, Control and Computing (ICSTCC)*, 2023.

[13] T. D. Tuttle and W. P. Seering, "A nonlinear model of a harmonic drive gear transmission," in *IEEE Transactions on Robotics and Automation*, vol. 12, no. 3, 1996, pp. 368–374.

[14] Schaeffler Technologies AG & Co. KG. Media library - precision strain wave gears RT1-T. Accesed: October 20, 2023. [Online]. Available: https://www.schaeffler.de/en/news_media/media_library/downloadcenter-detail-page.jsp?id=87820610

[15] A. Raviola, A. De Martin, R. Guida, G. Jacazio, S. Mauro, and M. Sorli, "Harmonic drive gear failures in industrial robots applications: An overview," in *Proc. of PHM Society European Conference*, vol. 6, no. 1, 2021, pp. 350–360.

[16] G. Yang, Y. Zhong, L. Yang, and R. Du, "Fault detection of harmonic drive using multiscale convolutional neural network," in *IEEE Transactions on Instrumentation and Measurement*, vol. 70, 2020, pp. 1–11.

[17] S. L. Brunton and J. N. Kutz, *Data-driven science and engineering: Machine learning, dynamical systems, and control*. Cambridge University Press, 2019.

[18] F. Pedregosa, G. Varoquaux, A. Gramfort, V. Michel, B. Thirion, O. Grisel, M. Blondel, P. Prettenhofer, R. Weiss, V. Dubourg, J. Vanderplas, A. Passos, D. Cournapeau, M. Brucher, M. Perrot, and E. Duchesnay, "Scikit-learn: Machine learning in Python," *Journal of Machine Learning Research*, vol. 12, pp. 2825–2830, 2011.

[19] M. J. Islam, Q. J. Wu, M. Ahmadi, and M. A. Sid-Ahmed, "Investigating the performance of naive-bayes classifiers and k-nearest neighbor classifiers," in *Proc. of 2007 International Conference on Convergence Information Technology (ICCIT)*, 2007, pp. 1541–1546.

[20] D. Anguita, L. Ghelardoni, A. Ghio, L. Oneto, S. Ridella *et al.*, "The'k'in k-fold cross validation." in *Proc. of 2012 European Symposium on Artificial Neural Networks, Computational Intelligence and Machine Learning (ESANN)*, 2012, pp. 441–446.